Materials Today Bio 27 (2024) 101117

Contents lists available at ScienceDirect

Materials Today Bio

journal homepage: www.journals.elsevier.com/materials-today-bio

Targeted therapy and deep learning insights into microglia modulation for spinal cord injury

Emilia Petillo [a,b,1], Valeria Veneruso [a,c,1], Gianluca Gragnaniello [d], Lorenzo Brochier [d], Enrico Frigerio [a], Giuseppe Perale [c,f,g], Filippo Rossi [b], Andrea Cardia [e], Alessandro Orro [d,*], Pietro Veglianese [a,c,**]

[a] Department of Neuroscience, Istituto di Ricerche Farmacologiche Mario Negri IRCCS, via Mario Negri 2, Milano 20156, Italy
[b] Department of Chemistry, Materials and Chemical Engineering "Giulio Natta", Politecnico di Milano, via Mancinelli 7, Milano 20131, Italy
[c] Faculty of Biomedical Sciences, Università della Svizzera Italiana, via Buffi 13, Lugano 6900, Switzerland
[d] Department of Biomedical Sciences, Italian National Research Council, Institute of Biomedical Technologies, Segrate 20054, Italy
[e] Department of Neurosurgery, Neurocenter of the Southern Switzerland, Regional Hospital of Lugano, Ente Ospedaliero Cantonale (EOC), Lugano, Switzerland
[f] Ludwig Boltzmann Institute for Experimental and Clinical Traumatology, Donaueschingenstrasse 13, 1200 Vienna, Austria
[g] Regenera GmbH, Modecenterstrasse 22/D01, 1030 Vienna, Austria

A B S T R A C T

Spinal cord injury (SCI) is a devastating condition that can cause significant motor and sensory impairment. Microglia, the central nervous system's immune sentinels, are known to be promising therapeutic targets in both SCI and neurodegenerative diseases. The most effective way to deliver medications and control microglial inflammation is through nanovectors; however, because of the variability in microglial morphology and the lack of standardized techniques, it is still difficult to precisely measure their activation in preclinical models. This problem is especially important in SCI, where the intricacy of the glia response following traumatic events necessitates the use of a sophisticated method to automatically discern between various microglial cell activation states that vary over time and space as the secondary injury progresses. We address this issue by proposing a deep learning-based technique for quantifying microglial activation following drug-loaded nanovector treatment in a preclinical SCI model. Our method uses a convolutional neural network to segment and classify microglia based on morphological characteristics. Our approach's accuracy and efficiency are demonstrated through evaluation on a collection of histology pictures from injured and intact spinal cords. This robust computational technique has potential for analyzing microglial activation across various neuropathologies and demonstrating the usefulness of nanovectors in modifying microglia in SCI and other neurological disorders. It has the ability to speed development in this crucial sector by providing a standardized and objective way to compare therapeutic options.

1. Introduction

Spinal cord injury (SCI) is the most debilitating condition of the cord. The primary damage provoked by the mechanical trauma is further worsened by a series of secondary neuropathological events that can take place over a protracted period of time after trauma limiting the recovery. Various pathophysiological mechanisms contribute to the secondary injury including hemorrhage, oxidative stress, inflammation, and excitotoxicity. Among them, inflammation is a key player in the dramatic evolution of tissue loss with a harmful or protective role depending on the environment cues [1–3]. Activated glial cells after the lesion are able to orchestrate many complex responses releasing inflammatory molecules [1] and contributing to the scar formation after the trauma [1,4].

Microglia are the resident immune cells of the central nervous system (CNS). They play a vital role in maintaining CNS homeostasis and responding to injury. In the context of SCI, microglia are activated and release a variety of factors that can either promote or inhibit repair [1]. The morphotype of microglia, or their physical appearance, is a determinant key of their function [5]. Resident microglia have a resting phenotype in the healthy CNS with a sprouted morphology with cytoplasmic processes able to monitor the microenvironment [5]. They are the first cells able to respond to the insult after the trauma, changing their morphology and becoming activated with thicker ramified processes and larger cell bodies [1]. Microglia extend their cytoplasmic processes towards the lesion and migrate in the epicenter of the lesion.

* Corresponding author. Department of Biomedical Sciences, Italian National Research Council, Institute of Biomedical Technologies, Segrate 20054, Italy.
** Corresponding author. Department of Neuroscience, Istituto di Ricerche Farmacologiche Mario Negri IRCCS, via Mario Negri 2, Milano 20156, Italy.
E-mail addresses: alessandro.orro@cnr.it (A. Orro), pietro.veglianese@marionegri.it (P. Veglianese).
[1] contributed equally.

https://doi.org/10.1016/j.mtbio.2024.101117
Received 2 May 2024; Received in revised form 31 May 2024; Accepted 8 June 2024
Available online 8 June 2024

During the progression of the secondary injury other different morphological states have been identified, such as phagocytic-like microglial cells showing a rod-shape strongly resembling macrophagic cells [1,5]. Recently, eleven different microglia phenotypes have been identified based on their transcriptional profile [4] and the different activation state of microglia is also recorded in its proliferation and progressive morphological transformation [1,5].

Traditional therapies that act on microglial cells frequently lack selectivity, resulting in limited efficacy or undesirable side effects [6]. Newer approaches try to precisely target microglia to either reduce detrimental inflammation or create a regenerative phenotype necessary for repair. This trend is consistent with our increased understanding of microglial heterogeneity and their various roles in neurodegeneration and healing. Nanovectors are one of the most promising targeted methods. These tailored nanoparticles can be functionalized to interact specifically with microglia, delivering therapeutic drugs directly to these important immune cells [7–10]. This selectivity has the potential to reduce off-target effects and increase therapy efficacy. This technique has several advantages: 1. Improved drug bioavailability; nanovectors can encapsulate diverse therapeutic compounds, keeping them from degradation and facilitating their distribution across biological barriers. 2. Improved cellular uptake, specific ligands on the nanovector surface can bind to microglia receptors, resulting in effective internalization and drug release within these cells. 3. Modulation of microglia polarization: nanovectors can be used to carry compounds that affect microglia phenotype, changing them toward a reparative state promoting tissue healing. By relying on these benefits, nanovectors have the potential to advance microglia-targeted therapeutics and improve outcomes for a variety of neurological conditions. In developing these effective immune-based therapies for microglia activation, it is difficult to demonstrate how the treatment affects the microglia response in terms of the number of cells involved and their spatial distribution, which, along with morphology, are all relevant indicators of the efficacy of microglia modulation following a treatment.

Within this framework, automated microglia detection is crucial for achieving reproducible and accurate assessment of treatment effects for several key reasons.

1. Tracking Microglia Activation Over Time: Automated detection enables reliable assessment of microglia activation changes over time, offering important insights into disease progression and therapy efficacy. This allows researchers to objectively evaluate the effects of interventions on inflammatory responses and microglial dynamics.
2. Identifying Microglia Subtypes: By precisely discriminating between distinct microglia subtypes based on morphology and marker expression, automated approaches can reveal the exact cell populations that are most affected by treatment. This critical knowledge can help us understand the mechanisms of action and lead the development of targeted medications.
3. Optimizing Subtype-Specific Therapies: Researchers can modify and optimize therapy techniques targeting certain subtypes by precisely quantifying and characterizing various microglia populations. This approach holds the potential for personalized medicine, tailoring treatments to target the most relevant cell populations in each patient.

Significant progress has been made in the development of automated approaches for characterizing and detecting microglial morphotypes [11–18]. Deep Learning (DL), specifically convolutional neural networks (CNNs), has been found to be extremely successful for automated detection of microglia morphotypes, with the ability to learn complicated features such as form, size, and texture. Although these developments show that automated approaches for recognizing microglia morphotypes are able to become more complex and reliable, they still fail to generate high-quality segmentation in tissue regions with high cell density or cell signal intensity overlap. As a result, the currently available techniques are primarily dependent on manual recording or semi-automated quantification of microglia, which is frequently incorrect, imprecise, and time-consuming.

In order to improve the accuracy, save time for the quantification of microglia in *ex vivo* tissue, and correlate these neuropathological events to the treatment action we developed a fully automated DL based software application, This application simplifies and ensures accurate microglial cell analysis after treatment with a drug-delivering nanovector in complex acute neurological conditions like SCI, with promising potential for application in various neurodegenerative diseases.

2. Methods

2.1. Nanoparticles synthesis

NG conjugated to RhB was synthesized according to the experimental procedure previously described [8,19–21]. Briefly, polyethylene glycol (PEG) hydroxyl groups were modified with imidazole moieties using 1,1′-carbonyldiimidazole (CDI) (PEG-CDI), and polyethyleneimine (PEI) chains decorated with propargyl groups were further functionalized through the copper-catalyzed azide-alkyne Huisgen cycloaddition reaction using Rhodamine B (RhB). Two solutions were prepared separately: the first solution was obtained by dissolving PEG-CDI (200 mg, 0.025 mmol) in CH_2Cl_2 (3 mL), and the second BMone by dissolving PEI conjugated with RhB (0.017 mmol) in distilled water (5 mL). Under vigorous stirring, the organic solution was added dropwise to the aqueous system, and the final blend was sonicated for 30 min. The polymeric solution was then stirred for 17 h at 25 °C with the gradual evaporation of CH_2Cl_2. The aqueous system was then purified through dialysis, and lyophilized, resulting in a red (NG-RhB) solid.

2.2. Animal Care

The Institute of Pharmacological Research Mario Negri IRCCS provides that all procedures comply with the principles established by the Italian Disciplinary Law (D.lgs 26/2014; Authorization n.19/2008-A issued March 6, 2008 by the Ministry of Health), the NIH Guide for the Care and Use of Laboratory Animals (2011 edition) and EU directives and guidelines (EEC Council Directive 2010/63/UE). In addition, the Institutional and Policy Regulation of Mario Negri ensures that people conducting experiments on animals have obtained the Certificate of the Quality Management System (UNI EN ISO 9001:2015, reg. n. 6121).

2.3. Surgery

B6.129P-Cx3cr1tm1Litt/J (The Jackson Laboratory) mice were used for *ex vivo* studies. Prior to surgery, the animals were given a subcutaneous dose of antibiotic (ampicillin 50 mg/kg) and an analgesic one (buprenorphine 0,15 mg/kg). Then the animals were placed in a chamber saturated with 2 % isoflurane in oxygen to induce deep anesthesia (about 5–10 min) maintained throughout the operation. The procedure was performed on a Cunningham spinal cord adaptor (Stoelting, Dublin, Ireland) mounted on a stereotactic structure. After performing laminectomy of the T12 vertebra, the spinal cord was exposed and compressed with an aneurysm clip (2Biological Instruments Snc, No. cat.14120) for 1 min and then removed, causing controlled mechanical trauma (constant closing force of 30 g). After the SCI, the dorsal muscles were juxtaposed using absorbable sutures and the skin was carefully sutured and disinfected.

The NG-Roli group was treated after 1 day post injury (DPI) with Rolipram, an anti-inflammatory drug, loaded with NG-RhB as previously demonstrated and characterized by our group [19]. Briefly, one day after the trauma, the spinal cord of injured mice was exposed and nanogel loaded with Rolipram was injected intraparenchymal. Six 0.250 μL injections were done with a glass capillary (outer diameter 40 ± 2 μm) to cover the injured area. The capillary was positioned ±0.5

mm from the midline, then it was deepened into the parenchyma to 0.6 mm below the pia mater. After the treatment, dorsal muscles were juxtaposed, the skin was sutured and disinfected.

The convalescent animals were placed in separate cages with food and water *ad libitum* and kept for observation by authorized personnel.

2.4. Spinal cord transcardial Perfusion

For histological and morphological analysis, deep anesthesia was induced fourteen DPI to the animals by intraperitoneal injection of ketamine hydrochloride (IMALGENE, 100 mg/kg) and medetomidine hydrochloride (DOMITOR, 1 mg/kg). Then they were transcardially perfused with 40 ml of 0.1 mol/L saline phosphate buffer (PBS), pH 7.4 for 4 min, followed by 50 ml of paraformaldehyde solution (4 %) in PBS for 5 min. The spinal cord was gently removed and post-fixed overnight in the same fixative at 4 °C, then transferred to 30 % sucrose in phosphate buffer 0.1 mol/L for correct cryopreservation and stored at 4 °C until use.

2.5. Immunofluorescence

The spinal cord was manually cut at 6 mm from the epicenter of the injury at both the rostral and caudal ends. The sample was embedded in OCT compound, promptly frozen in N-pentane at −45 °C for 3 min and stored at −80 °C until use. Tissues were sectioned at 30 μm using a cryostat at −22 °C and stored in PBS 0.01 M at 4 °C. The sections were sampled (one for each five) and separated. Nuclei were labeled with Hoechst (Hoechst33258 10 μg/mL, Invitrogen) and then, gently laid on microscope slides and covered with FluorSave Reagent (Millipore) before being acquired.

2.6. Microscopy

Tissue slices were acquired using a cellR microscope (Olympus) equipped with 20 × /0.70 air magnification and an ORCA camera (Hamamatsu). Each coronal section was acquired at 20x using a step size of 1 μm (4 z-stack).

2.7. Statistical analysis

We used Prism software (Graphpad) for statistical analyses. Mann−Whitney test and one-way ANOVA followed by Bonferroni's post-hoc test were used to see relative captions. Outliers will be calculated with the Grubbs' test (extreme studentized deviate) (Graphpad). P-value <0.05 will be considered as statistically significant for all analyses.

3. Results

3.1. Image pre-processing and DL segmentation

To evaluate the images for DL segmentation, we first preprocessed them. The size of the two acquired images is 5570 x 8587 pixels and 6506 x 8543 pixels, respectively. These images contain a green fluorescent channel for microglial cells, a blue fluorescent channel for nuclei from all the cells in the sample, and a z dimension representing the four slices into which the sample was cut. In each image, z-planes were fused by taking the most intense pixel in each plane. The images were then equalized with Contrast Limited Adaptive Histogram Equalization (CLAHE) to improve contrast in areas that were too dark or too light. Half of the second image was cropped and reserved for an unbiased final test. The rest of the data were divided into non-overlapping subsquares of 128x128 pixels. All subsquares that had an average signal intensity less than 0.02 were eliminated to prevent the signal-free regions from unbalancing the dataset too much. The 80 % of the subsquares were randomly assigned to the training set, while the remaining 20 % were assigned to the validation set.

To address the limitations of manual counting and enhance the efficiency of accurately identifying microglia, we evaluated and optimized various artificial intelligence architectures for predicting green fluorescent protein (GFP)-positive microglia in spinal cord sections following trauma induction at fourteen DPI. We processed spinal cord sections containing representative cell morphotypes identified by GFP signal constitutively expressed in microglia of B6.129P-Cx3cr1tm1Litt/J transgenic mice. We manually delineated the perimeter of microglial cells by tracing their outlines for both training and test images. Four state-of-the-art DL architectures (see Table 1) for quantitative image segmentation were evaluated and will be discussed in this paragraph.

Deep Learning Architectures used for image segmentation of microglia cells.

Unet [22] is the most widely used architecture for semantic segmentation (Fig. 1; a), and it is also the first to employ an encoder-decoder structure. The encoder reduces the spatial dimensions (height and width) of the input while simultaneously increasing its depth to extract relevant features (latent representation). Each encoder block consists of 2 convolutions (kernel size = 3x3) and a 2x2 max pooling with (stride = 2) to reduce the spatial dimensions and increase the receptive field. The latent representation is then processed by the decoder, an expansive upsampling path that restores that image to its original spatial dimension. For each decoder block, we employed a transpose convolution, which doubles the spatial dimensions and halves the depth before being concatenated with encoder features. This is followed by two 3x3 convolutions, followed by 2 convolutions with kernel size = 3x3. All convolutions in the network are followed by a ReLU activation function except the last layer, which consists of a sigmoid activation function to obtain the probability of each pixel belonging to class 0 or 1. Concatenating encoder features with decoder features, known as skipped connections, is a technique commonly used in medical image segmentation to enhance gradient flow during backpropagation and recover spatial information lost during downsampling.

To determine whether the nuclei channel could be utilized to improve segmentation accuracy, we attempted to modify *Unet* following the structure of the *FuseSeg* [23] architecture (Fig. 1; b) originally proposed to extract information from multi-channel images. In regions where nonspecific fluorescence is present, possibly due to instrumentation artifacts or autofluorescence, the presence or absence of a nucleus could provide the network with the discriminative power to accurately classify the region. We modified *Unet* by adding a second encoder module parallel to the first one, which takes the nuclei channel as input. In this manner, the two channels are processed independently before being summed and passed to the decoder, which is instead a single-path module. The features of the two encoders before each max pooling are summed and passed to the decoder as skipped connections. This approach aims to incorporate the nuclei channel's information into the segmentation process.

To assess the significance of scale in feature extraction, we evaluated a Dense Dilated Inception Network (*DDI-Net*) [24] architecture (Fig. 1; c) incorporating two modifications to the standard *Unet* architecture. Firstly, we replaced the *Unet* convolution blocks with Dilated-Inception blocks [26] comprising parallel 3x3 convolution filters with varying dilation rates. These blocks undergo concatenation and are further

Table 1

Unet [22]	a classic Encoder-Decoder scheme with simple convolution layers
FuseSeg [23]	a model that exploits two separate encoders to process microglia and nuclei channels
DDI-Unet [24]	an *Unet* extension where dilation rate is used in convolution layers for extracting features at different scales and skipped connections replaced with Dense-Path
DC-Unet [25]	an *Unet* extension where two MultiRes modules work in parallel for feature extraction at different scales and skipped connections replaced with Res-Path

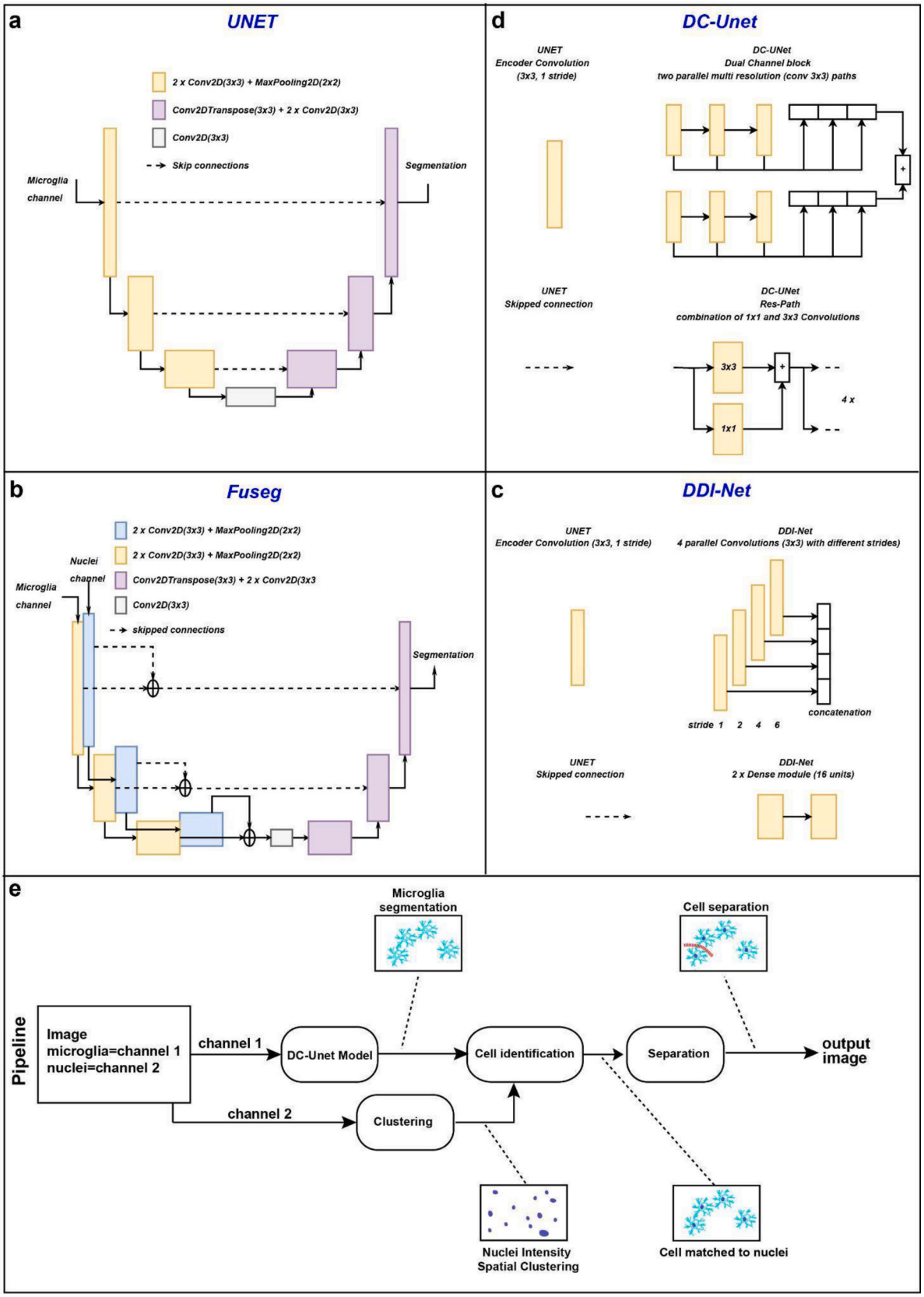

Fig. 1. Deep Learning architectures for image segmentation.
a) Standard Unet with skipped connections; b) Fuseg with two separated paths for microglia and nuclei channels; c) representation of the DDI-Net represented in terms of the two modules (4 parallel convolution layers with different strides and Dense-Path) that replace the corresponding modules of the Unet (convolution of the encoder path and the skipped connections); d), The DC-Unet represented in terms of the two modules (dual channel block and Res-Path) that replace the corresponding modules of the Unet. e) Schematic representation of the DL Pipeline based on DC-Unet segmentation, post-processing and clustering.

reduced in depth using a 1x1 convolution operation. The dilation rate expands the receptive field by increasing the spacing between each pixel in the convolutional filter, enabling the network to explore a broader spatial extent without enlarging the kernel size of the convolution layers, preserving the number of parameters. The second modification involves replacing the skipped connections with a sequence of dense modules (Dense-Path), which enhances the computational capacity of the decoders. This is crucial as the decoders process more intricate inputs than the encoders, bridging the semantic gap between the two modules.

The last architecture evaluated was *DC-Unet* [25] (Fig. 1; d), which builds upon the *Unet* framework by introducing modifications to address the challenges posed by features of varying sizes. Compared to the standard *Unet* architecture, *DC-Unet* employs a MultiRes module, comprising stacks of small 3x3 and 5x5 convolutions, replacing the single large convolutions of the original design. Additionally, it utilizes a Res-Path module, consisting of parallel 3x3 and 1x1 convolution blocks that are summed together before advancing to the next block, effectively replacing the standard skip connections and enhancing processing capabilities.

The implementation of all DL models was carried out from scratch, adhering to the fundamental principles of each architecture without utilizing pre-trained networks as backbones.

The performance of all models was assessed using four metrics: precision, recall, F1-score and accuracy being the first three the most pertinent for image segmentation tasks:

$$Accuracy = \frac{TN + TP}{P + N} \tag{1}$$

$$Recall = \frac{TP}{TP + FN} \tag{2}$$

$$Precision = \frac{TP}{TP + FP} \tag{3}$$

$$F1\ score = \frac{2TP}{2TP + FP + FN} \tag{4}$$

where TP, FP, FN, and TN are the pixel-based counts of true positives, false positives, false negatives, and true negatives, respectively. As usual in image segmentation problems, we adopted, for the backpropagation algorithm, a loss function based on the dice coefficient that measures the similarity between two images in terms of pixel overlapping.

$$loss = \frac{FP + FN}{2 \cdot TP + FP + FN} \tag{5}$$

Segmentations produced by DL models are susceptible to exhibiting minor artifacts due to equalization effects, autofluorescence, and tiling size. Often, these predictions fall under the category of false positives and require removal through a post-processing pipeline. The post-processing pipeline (Fig. 1; e) takes both the microglia and nuclei images as input, along with the segmentation predicted by the DL model. It considers four parameters to determine whether a prediction should be deemed a false positive and subsequently eliminated.

- Microglia area: The size in pixels of the predicted microglia area.
- Nuclei area: The size in pixels of the predicted nuclei area.
- Nuclei intensity: The intensity of the nuclei channel.
- Microglia intensity: The intensity of the microglia channel.

First, the nuclei image undergoes segmentation using a threshold to obtain nuclei positions. Subsequently, the predicted microglia cells (binary) of the model are multiplied with the "prediction" of the nuclei. This enables the retention of only core regions within the boundaries of the predicted microglia. At this point, for each predicted cell, the remaining parameters described above are compared against their respective thresholds. If even one of these parameters falls below its threshold, the cell is deemed a false positive and discarded.

Furthermore, the segmentation generated by the DL model exhibits suboptimal segmentation of the cells, stemming from challenges in recognizing morphology and a tendency to produce cells that are clumped together in regions of high intensity. To address this issue, a cell separation algorithm was implemented.

1. Initially, a cluster analysis was performed on the nuclei channel to identify genuine nuclei cells.
2. The identified nuclei cells were then superimposed onto the corresponding microglia/astrocyte cell channels.
3. A multi-step and multi-label dilation algorithm was employed, which starts at the nuclei boundaries and expands (dilates) the area until it encounters neighboring cells or the background. This step proved crucial in ensuring effective cell separation.

Following DL segmentation, the morphological analysis was performed by first computing morphological features (Table 2) of the cells. These features are then used to cluster the cells into groups using the k-means algorithm. The number of clusters is predefined to two (healthy mice) or three (injured mice), corresponding to the main microglial morphological types: *ramified* and *hyper-ramified* for spinal cord of healthy mice or *bushy*, *ameboid*, and *phagocytic-like* microglia for spinal cord of injured mice. Table 2 shows the features used in this analysis.

To compare the performance of the different architectures, we calculated the Precision, Recall, and F1 score metrics. The architecture *DC Unet* with an F1-score of 76.92 showed the best performance (Fig. 2). To gain a better understanding of the DL models, we compared them against some traditional thresholding techniques like Otsu [27] and against a manual curated annotation. All DL models outperform classical thresholding. The best traditional method is as expected the manual one, which however, on top of not getting close to DL models, requires manually setting a threshold that may be sample-specific.

These pictures compare the performance of four different DL segmentation architectures: Unet, FuseSeg, DDI-Unet, and DC-Unet. The architectures were evaluated on the same dataset of images. The performance of the architectures is evaluated using both validation (a) and thresholding comparison (b).

3.2. Validation of the morphometric detection of microglia in SCI spinal cord tissue by DL analysis

The DL based method for segmentation was validated against manual

Table 2

area (a)	number of pixels of the cell ara
perimeter (p)	number of pixel of the border of the cell area
normalized perimeter	p/a
convex hull area (ha)	number of pixels of the convex hull region
convex hull perimeter (hp)	number of pixels of convex hull region perimeter
convex hull normalized perimeter	hp/ha
convexity	hp/p
centroid	center of mass of the cell (uniform density)
solidity	a/ha
circularity	$4 * \pi * a/p^2$

Table shows the features applied: Area = The total area enclosed by the shape's boundary; Perimeter = The total length of the shape's boundary; Normalized perimeter = The perimeter divided by the area; Convex hull area = The area enclosed by the smallest convex hull that can be drawn around the shape; Convex hull perimeter = The total length of the boundary of the convex hull; Convex hull normalized perimeter = The perimeter of the convex hull divided by the convex hull area; Convexity = A measure of how closely a shape resembles its convex hull; Centroid = The geometric center of the shape; Solidity = A measure of how much of a shape is filled in; Circularity = A measure of how closely a shape resembles a circle.

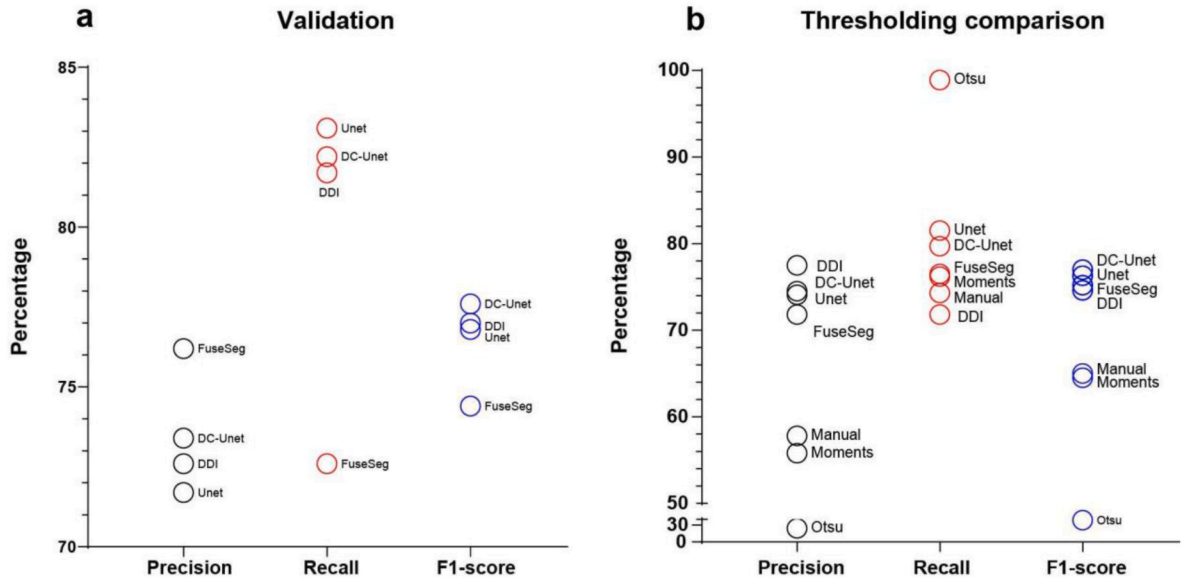

Fig. 2. Performance comparison of four different Deep Learning segmentation architectures.

annotations of microglia in the healthy spinal cord. Microglia were spatially distributed in the gray and white matter of the tissue sampled, preserving their own space (Fig. 3A; a,b). Microglia cells showed mostly a resting-surveillance ramified phenotype with a well-defined central body and longer ramifications, identified by a GFP positive staining, which is expressed under a specific microglia promoter, CX3CR1, which is one of the most commonly used labels of microglia (Fig. 3A; b,d). The cells manually annotated in 20 coronal spinal cord sections in a tract of about 3,5 mm (Fig. 3A; a), were compared to the number of microglia obtained with the automatic DL approach (Fig. 3A; b-g). Two independent observers performed the manual counting, which yielded a total number of approximately 500 cells per section (Fig. 3A; g). The total number of cells manually counted for each section was compared to the prediction obtained by DL analysis (DC-Unet), revealing a good correlation between the manual and automatic approaches, as expressed by linear regression (R squared 0.953) (Fig. 3A; g). After SCI, microglia became activated. They were characterized by their ameboid shape and short processes. Ameboid microglia are highly motile and can rapidly migrate to the site of injury (Fig. 3B; b,d). Once at the site of injury, ameboid microglia become phagocytic, with a rounded shape, and can phagocytose debris and damaged cells (Fig. 3B; b,d). The DL method was also validated after microglia activation in injured spinal cord tissue fourteen DPI. DL analysis against manual annotations will be conducted for 20 sections of a tract of about 3.5 mm (Fig. 3B; a-g). The observers yielded a number of approximately 100–1500 cells for sections in the epicenter of the injured spinal cord and from 3000 to 5000 cells in the rostral and caudal part of the spinal cord (Fig. 3B; g). The total number of cells manually counted for each section was compared to the prediction obtained by DL analysis (DC-Unet), revealing a good correlation between the manual and automatic approaches, as expressed by linear regression (R squared 0.981) (Fig. 3B; g).

In order to characterize the morphotype of microglial cells, we used the described DC-Unet pipeline for non-damaged or injured spinal cord. Different shape metrics were explored for single microglial cells (Fig. 3C; a): cell area, cell circularity, cell convexity, cell solidity, cell perimeter, convex hull area, and convex hull perimeter. Cell area of the GFP-positive cells correlated negatively with cell solidity, cell convexity, and cell circularity, but positively with cell perimeter, cell convex hull area, and convex hull perimeter (Fig. 3C; a) in both non-damaged (Fig. 3C; f) and injured spinal cord (Fig. 3C; g). Microglia present a morphometric resting state, with a ramified morphology, with a small soma and long, branched processes that extend throughout the surrounding tissue in the injured tissue. These processes are constantly sampling the microenvironment for signs of damage or infection. Microglia are more densely distributed in the gray matter than in the white matter. They are also more densely distributed in the dorsal horn than in the ventral horn. Deeply investigating the morphological differences among the microglial cells recorded, we could identify two different populations of cells for the healthy spine after cluster analysis performed taking into account the previously seven metrics and applying an unsupervised K-means clustering: *Ramified cells* (cluster 1), these cells showed shorter branched processes with high cell circularity, cell convexity, and cell solidity. *Hyper-ramified* cells (cluster 2), these cells had higher cell area, cell perimeter, cell convex hull area, and convex hull perimeter (Fig. 3C; b,d). The results obtained by the DL pipeline subsequently processed by cluster analysis identified three different groups of cells in SCI sections, which can be classified as: *Phagocytic-like* cells (cluster 3), these cells were the clearly predominant cell type in the highly damaged area. They showed round shape phenotypes and higher solidity, circularity, and convexity (Fig. 3C; c,e). *Ameboid cells* (cluster 4) displayed a greater area than phagocytic-like cells, with higher cell perimeters, cell convex hull area, and convex hull perimeter, but lower cell solidity, cell convexity, and cell circularity (Fig. 3C; c,e). A lower number of cells was instead found for the morphotype identified as cluster 5, *bushy* cells (cluster 5), which represents a more ramified cell with reduced cell solidity, circularity, and convexity and conversely higher cell area, perimeter, convex hull area, and convex hull perimeter than cluster 3 and 4 (Fig. 3C; c,e).

To validate the capability of the DL pipeline to accurately predict the number and morphometric state of microglia in the injured spinal cord, we manually annotated the shape of microglial cells by drawing their outlines. Three sections were sampled from the rostral, epicenter, and caudal tracts of the spinal cord retrieved from a SCI mouse at fourteen DPI. We measured the error as the rate of false positives (overdetection of microglia) and false negatives (non-detection of microglia). The results showed that the error was mostly due to false positives, with a rate of $+10.27 \pm 0.83$ % (mean $\pm$ SD), compared to a false negative rate of $+0.78 \pm 0.39$ % (mean $\pm$ SD) (Fig. 4a). False positives were likely due to the separation of cells. The substantial presence of overlapping nuclei in the injured epicenter zone, which can cause a single cell to be split into multiple fragments. This can increase the number of cells detected by DL segmentation. We also compared the six metrics of the cells manually recorded with the automatic predictions achieved by the DL approach. This showed a good relationship between the trends for each feature

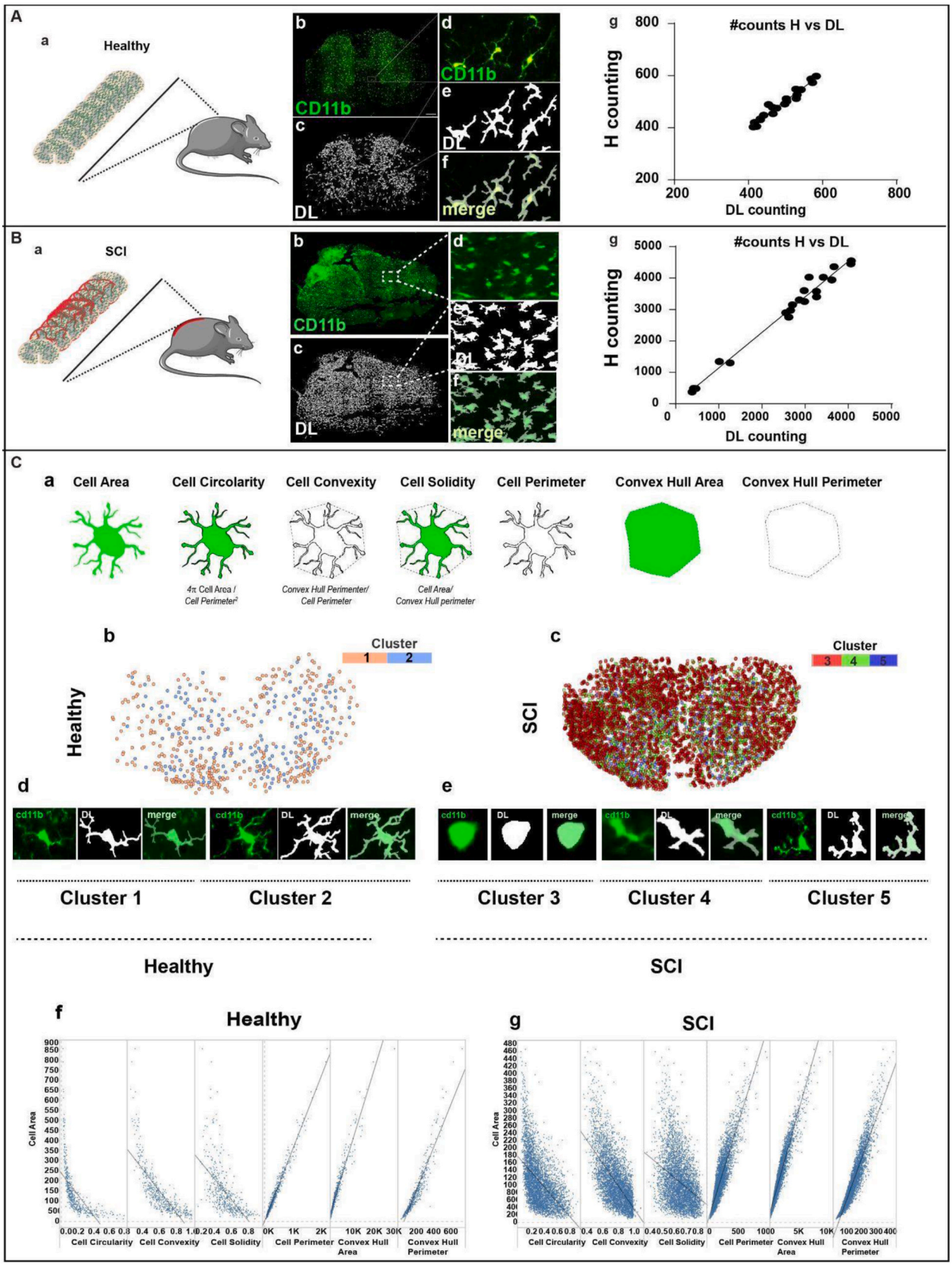

Fig. 3. Representative image of deep learning-predicted segmentation.

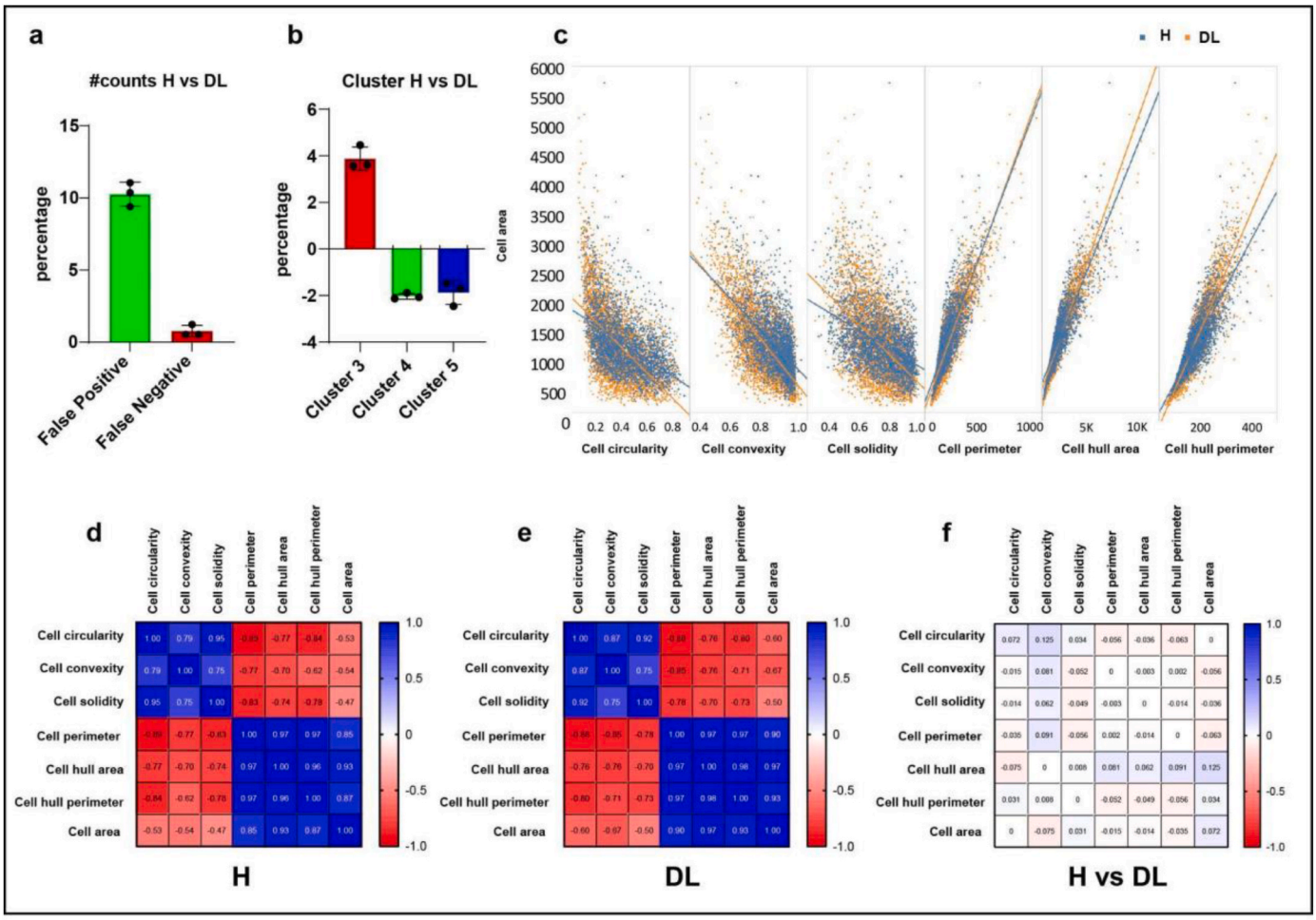

Fig. 4. Comparing and validating manual vs. deep learning evaluation.

evaluated (cell area/cell circularity, human R-squared = 0.248 vs DL R-squared = 0.341; cell area/cell convexity, R-squared = 0.318 vs DL R-squared = 0.489; cell area/cell solidity, R-squared = 0.274 vs DL R-squared = 0.204; cell area/cell perimeter, R-squared = 0.693 vs DL R-squared = 0.823; cell area/convex hull area, R-squared = 0.790 vs DL R-squared = 0.892; and cell area/convex hull perimeter, R-squared = 0.714 vs DL R-squared = 0.673) (Fig. 4; c).

We also evaluated the number of different microglia morphotypes found after DL analysis against manual annotation. This showed a rate of +3.88 ± 0.50 % (mean ± SD) for cluster 3, -2.03 ± 0.13 % (mean ± SD) for cluster 4, -1.87 ± 0.51 % (mean ± SD) for cluster 5. These results suggest that the cluster analysis of activated microglial cells is more accurate than cell counting. In addition, correlation analysis was performed for all shape metrics using Spearman's rank correlation methods. The results are represented as positive (red) or negative (blue) for the total of cells manually annotated (Fig. 4; d) or segmented by DL (Fig. 4; e). Differences between the two are shown in Fig. 4; f. This result suggests that comparable results were achieved when comparing the human evaluation to the DL analysis.

Representative spinal cord sections stained with CD11b of healthy (A) and injury (B) mice (b,d) with the corresponding DL segmentation analysis (c,e) and the merged image of CD11b staining and DL prediction (f); Correlation analysis between the number of cells detected by manual annotation and DL analysis is presented for 20 sections distributed rostrocaudally in the thoracolumbar spinal cord tract of injured mice (B; g) and the corresponding tract of healthy mice (A; g); (C) Distinct clusters of microglia were identified in healthy (cluster 1: ramified and cluster 2: hyper-ramified, b,d) and injured (cluster 3: phagocytic, cluster 4: ameboid, cluster 5: bushy, c,e) spinal cord tissues. These clusters are based on the morphological features of cell area, circularity, convexity, solidity, perimeter, and convex hull area (a) and are represented as dot plots that show the distribution of these features for single cells in healthy mice (f) and injured mice (g).

The figure compares the false positive and false negative rates of manual (human, H) vs. DL evaluation (a-c); Spearman correlation analysis (positive, red and negative, blu) among the morphological features cell area, circularity, convexity, solidity, perimeter, and convex hull area is represented for the manual annotation (d) and DL analysis (e), and shown as differences between the value recorded for the manual and DL analisis for each comparison (f). Data are mean ± SD. N = 3.

3.3. *Automated morphometric analysis of microglia in SCI spinal cord tissue section*

Once the model's predictions were validated, we analyzed larger areas of the injured spinal cord. We recorded the number of microglia cells distributed in 20 sections of injured spinal cord on fourteen DPI from the trauma induction and compared it to an equivalent tract of an intact spinal cord (Healthy). We compared the number of cells in a region of the spinal cord of approximately 3,5 mm in length of an healthy animal (Fig. 5) compared to 3 different injured animals (Fig. 6) to detect the increment of microglia in tissue of animals that underwent the acute trauma. Sections (30 μm thickness) were sampled one out of every five rostrocaudally, which includes the epicenter of the injury of the spinal cord tissue, corresponding to a spinal cord tract of approximately +1.5/−1.3 mm in dimension (T10-L1). DL counting demonstrated an

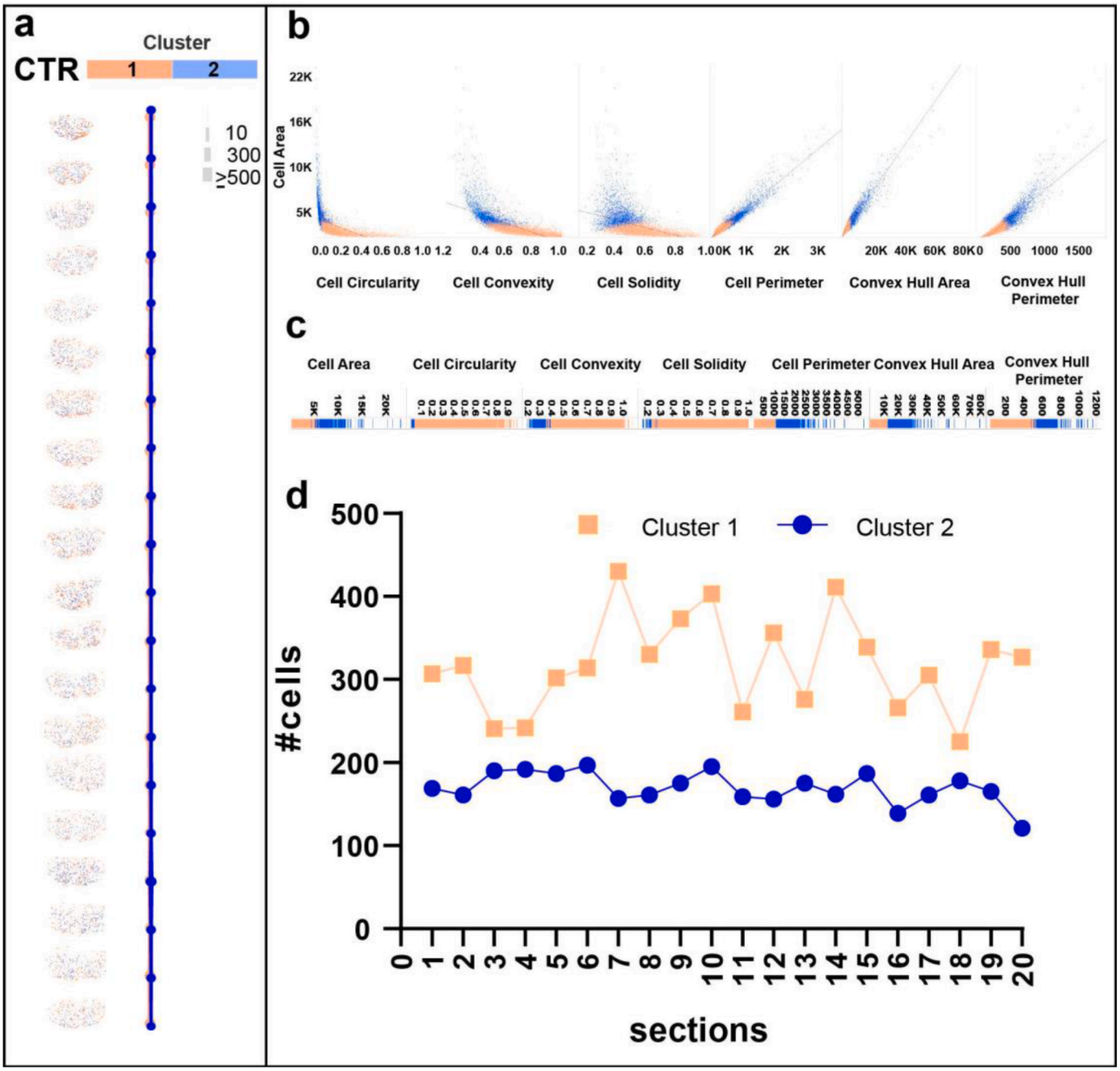

Fig. 5. Representative image of cluster analysis of microglia in a healthy spinal cord.
(a) The figure depicts a representative image of cluster analysis of microglia in a healthy spinal cord; (b,c) The analysis identified two distinct clusters of microglia based on their morphological features: ramified (a, cluster 1, ochre) and hyper-ramified microglia (a, cluster 2, blue). These clusters were differentiated based on quantitative parameters such as cell area, circularity, convexity, solidity, perimeter, and convex hull area; (d) A total of 20 sections were analyzed across the thoracolumbar spinal cord tract, and the relative number of each microglial morphotype. Data are mean ± SD. N = 3. (For interpretation of the references to color in this figure legend, the reader is referred to the Web version of this article.)

increased number of cells compared to the undamaged tissue in rostral and caudal sections (Fig. 6; a), an augment that reached ten fold compared to the same tract of undamaged spinal cord which showed about 500 cells/section (Fig. 5; a,d). This was quantitatively shown by the total number of cells recorded (Figs. 5 and 6; a,d). The number of microglial cells progressively decreased in the epicenter of the injury with a consistent reduction of the number of cells (Fig. 6; a). To identify single cells with different cell shape metrics we explored microglia phenotype at a single-cell resolution preserving cellular spatial relationships by DL analysis. Six metrics as described in the previous analysis (section 3.2) were explored: *cell area, cell circularity, cell convexity, cell solidity, cell perimeter, convex hull area, and convex hull perimeter*. These metrics were then processed by cluster analysis identifying two different morphological signatures in the spinal cord of the undamaged tissue: *hyper-ramified* cells (about 35 % of the total cells, cluster 2), were greater distributed in the gray matter, and *ramified* cells (cluster 1), corresponded to 65 % of the total cells, and mostly found in the dorsal horn of the gray matter and in white matter (Fig. 3C; b,d). Spinal sections derived from mice subjected to traumatic damage showed greater numbers of *phagocytic-like* cells, which are the most common cell type in the rim of the highly damaged area (Fig. 6; a-d). *Ameboid-like* cells were mostly distributed between the epicenter and the

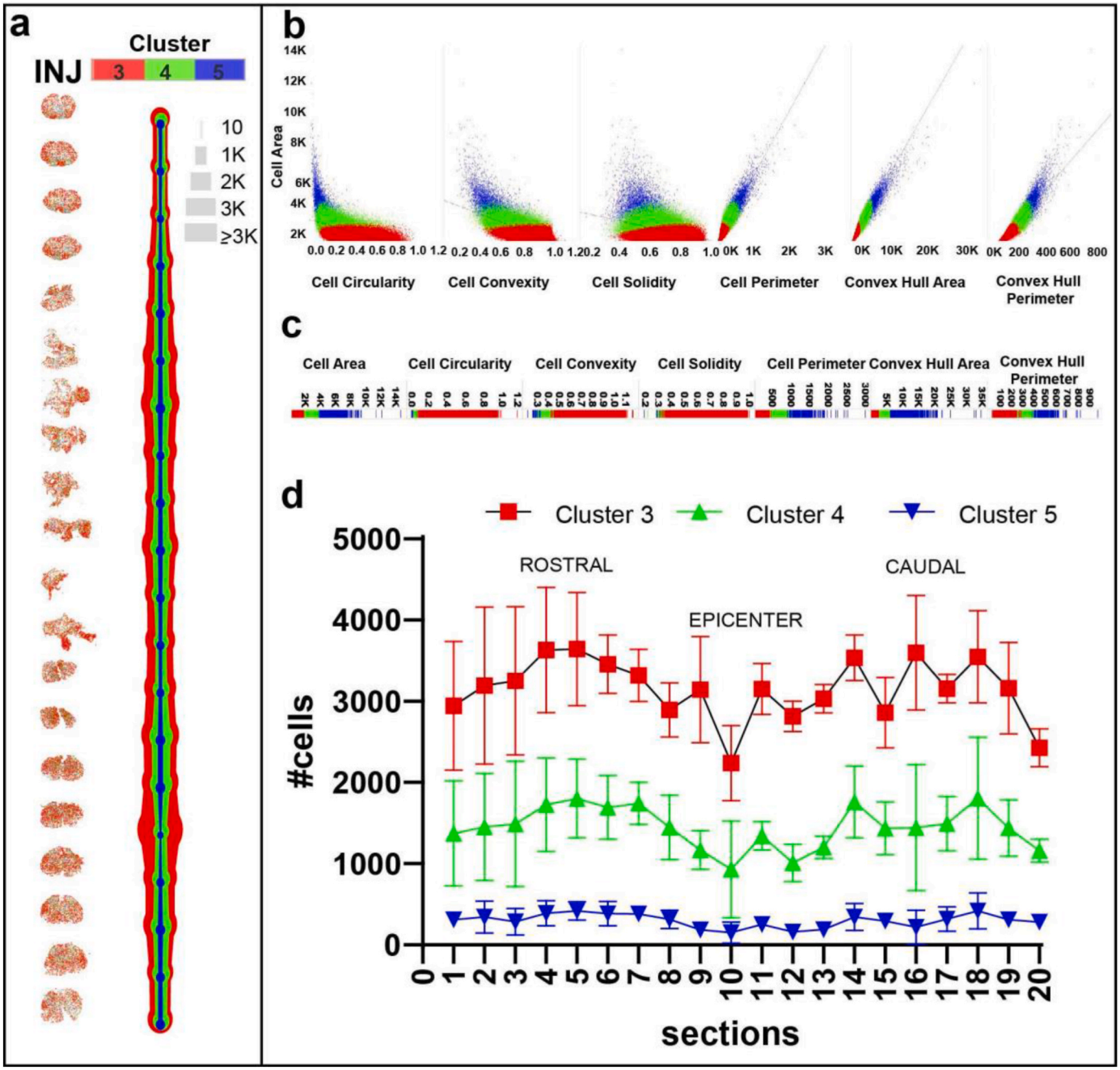

Fig. 6. Representative image of cluster analysis of microglia in an injured spinal cord.
(a) The figure depicts a representative image of cluster analysis of microglia in an injured spinal cord on fourteen DPI. The analysis identified three distinct clusters of microglia based on their morphological features: phagocytic (cluster 3, red) and ameboid (cluster 4, green) and bushy microglia (cluster 5, blue); (b,c) Clusters were differentiated based on quantitative parameters such as cell area, circularity, convexity, solidity, perimeter, and convex hull area; (d) A total of twenty sections were analyzed across the thoracolumbar spinal cord tract, and the relative number of each microglial morphotype. Data are mean ± SD. N = 3. (For interpretation of the references to color in this figure legend, the reader is referred to the Web version of this article.)

edge of the rostral and caudal tract (Fig. 6; a-d). The *bushy* cells had a comparable number of cells in the entire rostral-caudal direction (Fig. 6; a-d).

3.4. Morphometric analysis of microglia after a selective treatment by Rolipram loaded nanoparticles in SCI spinal cord tissue section

Rolipram, a phosphodiesterase type 4 inhibitor, has emerged as a promising therapeutic candidate for SCI due to its neuroprotective and anti-inflammatory properties [19,28,29]. Nanogels are hydrogel-based nanoparticles that can encapsulate and deliver drugs in a controlled and sustained manner [20,21,30,31]. This localized delivery approach ensures that therapeutic concentrations of Rolipram are maintained at the injury site, minimizing systemic side effects and enhancing its therapeutic efficacy [19,28].

Several studies have demonstrated the feasibility of using nanogels to deliver therapeutic agents to microglial cells in the spinal cord following intraparenchymal injection [19,20]. Our groups developed a nanogel system encapsulating Rolipram and demonstrated previously its effective internalization by microglial cells in a mouse model of SCI [19].

In this part of the study, we evaluated the capability of Rolipram-

loaded nanogel to modify the morphotype of microglia. Six injections of Rolipram-loaded nanoparticles were administered into the injured spinal cord one DPI (see methods), and the microglial morphological response was evaluated at fourteen DPI. Analyzing the total number of cells detected in a spinal cord tract of about 3.5 mm (Fig. 7; a-d), a significantly reduced number of cells was detected after Rolipram treatment compared to untreated injured spinal cord (Fig. 8; a,b). A more thorough analysis has shown that a reduced number of microglial cells was mostly detected in the farthest rostral and caudal tracts of the spinal cord compared to the epicenter (Fig. 8; a). This suggests that Rolipram-loaded nanogels confine microgliosis to the epicenter of the lesion, potentially reducing widespread degeneration. Additionally, cluster analysis revealed that phagocytic (cluster 3) microglia (Fig. 8; c, d) remain higher expressed in the tract of the spinal cord analyzed compare to ameboid morphotype (cluster 4) (Fig. 8; e,f), and less expressed is the bushy microglia (cluster 5) (Fig. 8; g,h). A quantitative analysis revealed a substantial decrease in the number of cells belonging to clusters 3 (phagocytic cells) (Fig. 8, c-d), 4 (ameboid cells) (Fig. 8, e-f), and 5 (bushy cells) (Fig. 8, g-h). This reduction was particularly pronounced in the most distal rostral and caudal regions of the spinal cord tract (Fig. 8; c,e,g). These findings demonstrate that Rolipram treatment effectively diminishes the population of phagocytic, ameboid, and bushy cells within the spinal cord. This suggests that nanogel-encapsulated Rolipram could serve as a promising therapeutic strategy for SCI by effectively targeting microglial cells and altering their morphology and function to promote recovery.

4. Discussion

In neurological conditions like SCI, understanding the complex role of microglia and their response to specific treatments is critical. However, achieving accurate and reproducible quantification of their modulation remains a significant challenge. This necessitates a robust and automated tool for several crucial reasons: firstly, reproducible microglia quantification ensures consistency across studies and laboratories. This facilitates data comparability and advances research knowledge, ultimately leading to a better understanding of microglia behavior in SCI. Secondly, a reliable tool empowers researchers to dig deeper into the intricate effects of targeted treatments. Tracking subtle changes in microglia number, morphology, and activation states is paramount, unlocking insights into the treatment's mechanisms of action and potential side effects. This level of detail informs the optimization of existing therapies and the development of more precise and effective approaches.

Quantifying microglia is challenging due to their small size, complex shape, and the need for high-resolution imaging. In addition, microglial morphology can vary depending on the state of activation of these cells. In a resting state, microglia have a small number of processes extending from their nucleus and appear rounded in shape. When activated, these cells can become highly ramified. Microglia can be divided at least into four distinct morphological types: inactivated-surveillant, ramified, ameboid like and phagocytic like. Their changeable morphology is strongly implicated as active participants in SCI neuropathology and their proliferation and changeable morphology is strictly linked with their functions during the progression of the secondary injury [1–3]. Interpreting the morphology of microglia is important for understanding their role and how they contribute to the progression of the secondary injury after SCI. Indeed, this difference in count and shape of microglia is important for helping to understand how they interact with each other and how they are responsive to different tested treatments.

Microglia cells play an important role in the spinal cord tissue after the acute injury event and their distribution and number can vary rostrocaudally [2–4,32–34]. Studies have shown that adopting an ameboid morphology microglia release proinflammatory cytokines, reactive oxygen species, and proteases [35]. These inflammatory mediators contribute to secondary neuronal damage, exacerbating the extent of tissue injury. The excessive production of ROS can lead to oxidative stress, damaging cellular components and impairing neuronal function [35]. On the other side microglia has demonstrated beneficial effects: microglia cells are responsible for protecting the tissue from damage, providing essential immune support, and helping to reduce the widespread distribution of the degenerative environment after SCI [4,35]. Consequently, quantifying microglial cells in distinct spinal cord segments can offer valuable insights into their role following spinal SCI. Moreover, comprehending the precise distribution and abundance of microglial cells across all regions of the spinal cord is crucial for evaluating the efficacy of proposed treatment strategies for spinal cord repair.

Manual counting of microglia has been used in many studies, but it is time consuming and prone to bias. This is typically done by examining slides under a microscope and manually counting each cell by using free ImageJ software and/or Sholl analysis approach [36]. Manual counting requires significant time and effort to complete as each cell must be counted individually. Additionally, manual counting can be subjective, as different researchers may count the same cells differently and often do not allow for a detailed analysis of morphological features, leading to inaccurate results. To address these issues, automated image processing tools are needed to accurately quantify microglial number and morphology.

The present study successfully proposes and investigates a robust discriminative machine learning model based on DL to predict distribution and morphology of activated microglia in an acute damaged spinal cord tissue. In addition this analysis properly allow the assessment of the fine ramification of different focal planes, indeed the microglial cell is a three-dimensional objects which requires a volumetric characterization, while many studies only used a two-dimensional approach for the image acquisition and subsequent image processing that does take in account all the future the volumetric shape of the microglia cells.

We investigated the number of microglia cells recorded as a fluorescence signal GFP expressed under a specific microglia/macrophage promoter, CX3CR1, which is one of the most commonly used labels of microglia [37]. Other studies demonstrated to record the number and morphology of microglia [36], but the present study is the first to successfully investigate automated number and morphology of microglia/macrophages in the SCI spinal cord section by a DL approach with both speed and reliability. Indeed, the complexity of the glia response generated after traumatic events such in SCI needs a sophisticated approach to automatically distinguish different states of activation of the microglial cells that change spatially and during the time in the secondary injury progression. One of the most widely used architectures for image segmentation is *Unet*, a CNN with a U-shaped structure that combines encoder and decoder paths. *Unet* has demonstrated remarkable performance in various segmentation tasks [22]. In this study we explored modifications to the *Unet* architecture to try to enhance its segmentation accuracy testing: *FuseSeg* [23], a variant of *Unet*, employs two separate encoders to process and fuse microglia and nuclei channels independently. This strategy effectively integrates the complementary information from both channels, leading to improved segmentation results. *DDI-Unet* [24], another variant, introduces dilation rate in convolutions to extract features at different scales. Additionally, it replaces skipped connections with Dense Path, which enhances feature propagation and alleviates the vanishing gradient problem. *DC-Unet* [25], a more recent architecture, incorporates two MultiRes modules in parallel to extract features at different scales. Similar to *DDI-Unet*, it replaces skipped connections with Res Path, further improving feature propagation and segmentation accuracy.

Despite the remarkable advancements in DL-based segmentation algorithm, it could still produce artifacts, particularly when trained on limited datasets or when encountering large high-intensity regions. To address this issue, this study applied a post-processing pipeline specifically designed to accurately cluster and differentiate cells from

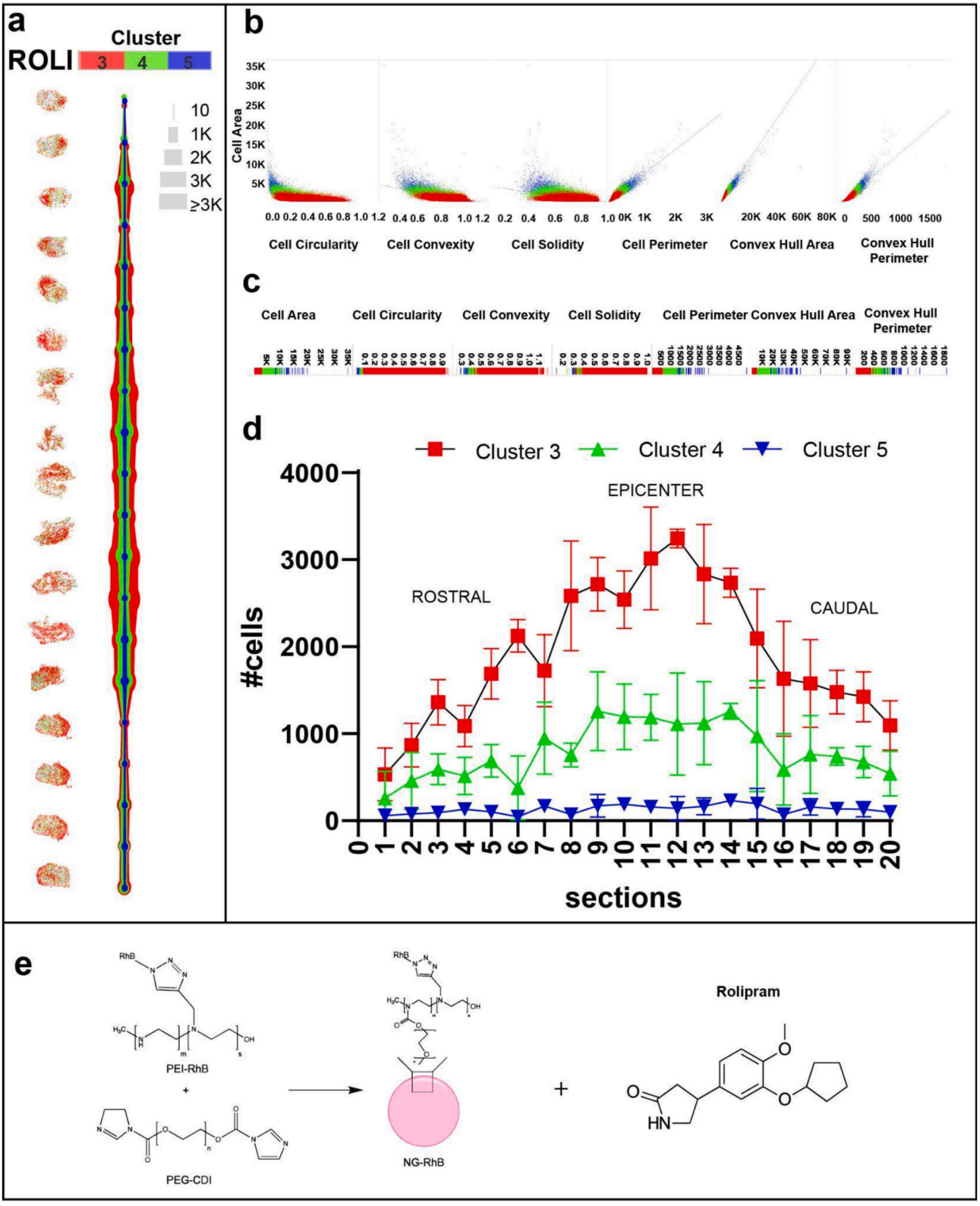

Fig. 7. Representative image of cluster analysis of microglia in an injured spinal cord at fourteen DPI following treatment with Rolipram-loaded nanoparticles administered at one DPI.

(a) The figure shows a representative image of cluster analysis of microglia in an injured spinal cord at fourteen DPI following treatment with Rolipram-loaded nanoparticles administered at one DPI. The analysis identified three distinct clusters of microglia based on their morphological features: phagocytic (cluster 3, red) and ameboid (cluster 4, green) and bushy microglia (cluster 5, blue); (b,c) Clusters were differentiated based on quantitative parameters such as cell area, circularity, convexity, solidity, perimeter, and convex hull area; (d) Synthesis of nanogel with rhodamine B-labeled PEI (PEI-RhB) conjugate with polyethylene glycol-carbonyldiimidazole (PEG-CDI), and Rolipram Loading (e). A total of twenty sections were analyzed across the thoracolumbar spinal cord tract, and the relative number of each microglial morphotype. Data are mean ± SD. N = 3. (For interpretation of the references to colour in this figure legend, the reader is referred to the Web version of this article.)

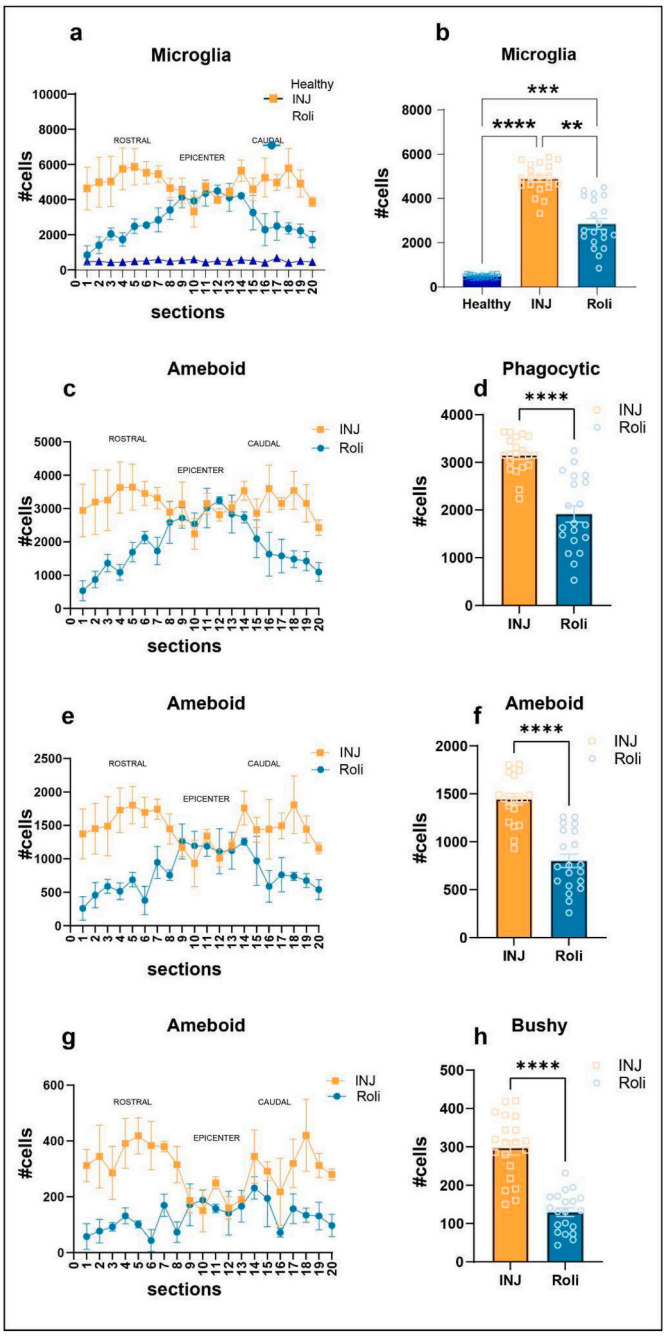

Fig. 8. Representative image of the number of microglia recorded rostrocaudally in the spinal cord of mice treated with Rolipram-loaded nanoparticles.

(a) Twenty coronal sections of the spinal cord of healthy (blue line), untreated (orange line), and Rolipram-treated mice (cyan line) are shown. There is a significant reduction in the total number of microglia (b), primarily in the outer rostral and caudal tracts, but not in the epicenter, of the spinal cord of Rolipram-treated mice compared to untreated mice. The sections analyzed in the outermost part of the spinal cord show a quantity of microglia comparable to that of the healthy mouse; Different clusters of microglia: phagocytic (c,d), ameboid (e,f), and bushy (g,h), have been analyzed. Phagocytic cells are more abundant in all sections analyzed, followed by ameboid cells (e,f), and the least prevalent are bushy cells (g,h). A significant proportional reduction was observed for all identified morphologies in the spinal cord of Rolipram-treated mice compared to untreated mice (c–h). Statistical significance: (**) $p < 0.01$; (***) $p < 0.001$; (****) $p < 0.0001$. one-way ANOVA (b); Mann-Whitney test (d,f,h). Data are mean ± SD. N (a, c, e, g) = 3; N (b, d, f, h) = 20. (For interpretation of the references to color in this figure legend, the reader is referred to the Web version of this article.)

artifacts. This pipeline effectively eliminates artifacts while preserving the integrity of cellular structures, thereby improving the overall segmentation accuracy and robustness of the DL model.

A comprehensive evaluation of the proposed DL architectures has shown that *DC-Unet* outperforms the others in terms of F1 score, a metric that balances precision and recall. This improved performance is attributed to the combination of MultiRes modules and Res Path, which effectively extract and propagate features at different scales, leading to more accurate segmentation of microglia in the tissue images. So, *DC-Unet*, with its robust architecture and superior performance, has emerged as a promising tool for automated microglia segmentation. Comparing the manual microglia recording with our DL approach is a reliable and efficient way to compare accuracy and precision. Therefore, we demonstrated that our DL prediction offers an acceptable accuracy and precision to manual recordings. We shown that a certain percentage of false positive (approximately 10 %) or negative (approximately 1 %) have been recorded in the number of microglia counted comparing manual annotation to DL analysis, likely due to the presence of overlapping nuclei in the injured epicenter zone, which can cause a single cell to be split into multiple fragments. This can increase the number of cells detected by DL segmentation increasing the false positive after DL analysis. We examined various shape measurements of individual microglial cells, including cell area, circularity, convexity, solidity, perimeter, convex hull area, and convex hull perimeter. They found that the cell area of GFP-positive cells was inversely related to solidity, convexity, and circularity, but directly proportional to perimeter, convex hull area, and convex hull perimeter in both undamaged and injured spinal cords. These morphological changes reflect the dynamic nature of microglial cells and their ability to adapt to different environmental conditions such as previously described [1]. By implementing this morphometric analysis, we demonstrated a significant reduction in error when evaluating the number of microglial cell morphotypes. Specifically, we observed a 4 % increase in the accurate identification of morphotype 3 cells, a 2 % decrease in errors for morphotype 4 cells, and a 2 % decrease in errors for morphotype 5 cells.

Overall, these findings suggest that replacing traditional manual microglial recording with a DL approach could offer significant advantages in terms of time efficiency (reducing the annotation time from three days for manual counting of all cells in a coronal section of spinal cord near the injured site to 5 min for DL prediction and cluster analysis), accuracy, and precision.

Analysis of 20 sections of the injured spinal cord using *DC-Unet* based DL revealed an increased presence of microglia distributed along the rostrocaudal axis of the spinal cord in SCI mice compared to healthy tissue. Microglia exhibited a pronounced accumulation in regions surrounding the epicenter of the injury, extending towards both rostral and caudal tracts of the spinal cord. In healthy tissue, we demonstrated that microglia are typically found in low numbers, with small, round cell bodies and process extensions. Cluster analysis revealed two distinct microglial morphotypes in healthy tissue: *hyper-ramified* and *ramified.* These morphotypes exhibited differential distribution patterns, with *ramified* microglia being more abundant in the white matter and dorsal horn of the gray matter. Conversely, in injured tissue, microglia displayed a larger cell size and reduced branching processes, adopting *phagocytic*, *ameboid*, or *bushy* phenotypes. The number of microglia in injured tissue was also significantly higher (approximately tenfold) compared to healthy tissue.

DL-based approaches have also been employed to assess microglia density and morphology after treatment with Rolipram-loaded nanoparticles, which selectively target the inflammatory state of microglia. These assessments were conducted in comparison to both healthy and diseased spinal cord tissues. These studies have consistently demonstrated a significant reduction in microglia number, particularly in the rostral (upper) and caudal regions (lower) of the injured spinal cord, following SCI. This microglial loss is accompanied by morphological alterations, including a shift towards a more ramified morphotype.

However, a higher number of cells remain around the epicenter of the lesion, suggesting a role in reducing the widespread degeneration of the lesion, while a reduced inflammatory effect is observed in the outer part of the lesion, as evidenced by a reduced activated morphotype.

Overall these data suggest that DL-based microglial cell quantification offers several advantages over traditional manual counting methods, especially when followed with a suitable post-processing analysis: the DL model can process large datasets of images efficiently and consistently, reducing the time and effort required for analysis. Additionally, DL models can objectively identify and count microglial cells, minimizing the subjectivity and errors inherent in manual counting methods. Furthermore, DL models can be trained to detect subtle morphological changes in microglial cells, providing valuable insights into their functional status. Based on morphological characteristics, this study distinguished five different microglial clusters, offering important information about the activation states of microglia. However, it's important to acknowledge limitations. The current approach may not capture the full spectrum of microglial heterogeneity within the injured spinal cord. Additional microglial subgroups with unique morphologies and functions could potentially exist. To address this limitation, future studies will explore incorporating additional metrics or markers into the clustering analysis: This would include measuring the intricacy of branching microglial processes in addition to their present physical characteristics. Examining the expression of genes associated with specific microglial functions [4] in conjunction with morphological data can be accomplished by using techniques like spatial transcriptomics, which allows us to link gene expression patterns to specific locations within the tissue. By incorporating these refinements, we aim to achieve a more comprehensive understanding of the various microglial responses following SCI.

To enhance the generalizability of our DL technique, we are actively investigating its applicability to microglia stained with more widely used markers, such as TMEM119, a specific microglial marker, CD11b, a marker expressed by microglia and other immune cells, and Iba1, another marker highly expressed by microglia. Including these markers will allow us to assess whether the technique can be adapted for broader use where GFP-expressing microglia might not be utilized.

In conclusion, DL techniques have emerged as a powerful tool for evaluating the microglial cell number and morphotype in SCI tissue sections after a selective delivery of drug by nanovectors. By utilizing the DL model trained on diverse datasets, researchers can accurately quantify microglial cells and gain insights into their morphological changes under various conditions of treatment. This approach holds promise for advancing our understanding of microglial cell biology, modulation and their contributions to CNS disease.

CRediT authorship contribution statement

Emilia Petillo: Writing – original draft, Validation, Methodology, Investigation, Conceptualization. **Valeria Veneruso:** Writing – original draft, Validation, Methodology, Investigation, Conceptualization. **Gianluca Gragnaniello:** Software, Methodology, Conceptualization. **Lorenzo Brochier:** Software, Methodology, Conceptualization. **Enrico Frigerio:** Methodology, Investigation. **Giuseppe Perale:** Writing – review & editing, Funding acquisition, Conceptualization. **Filippo Rossi:** Writing – review & editing, Writing – original draft, Methodology, Investigation, Conceptualization. **Andrea Cardia:** Writing – review & editing. **Alessandro Orro:** Writing – review & editing, Software, Methodology, Funding acquisition, Formal analysis. **Pietro Veglianese:** Writing – review & editing, Writing – original draft, Supervision, Investigation, Funding acquisition, Formal analysis, Conceptualization.

Declaration of competing interest

The authors declare that they have no known competing financial interests or personal relationships that could have appeared to influence the work reported in this paper.

Data availability

Data will be made available on request.

Acknowledgement

The authors' research was supported by Swiss project Innosuisse 59351.1 IP-LS, by Italian project CNRBIOMICS PON R&I PIR01_00017, and by the Amici del Mario Negri charity.

References

[1] Y.-P. Fang, Z.-H. Qin, Y. Zhang, B. Ning, Implications of microglial heterogeneity in spinal cord injury progression and therapy, Exp. Neurol. 359 (2023) 114239, https://doi.org/10.1016/j.expneurol.2022.114239.

[2] C. Zhang, J. Kang, X. Zhang, Y. Zhang, N. Huang, B. Ning, Spatiotemporal dynamics of the cellular components involved in glial scar formation following spinal cord injury, Biomed. Pharmacother. 153 (2022) 113500, https://doi.org/10.1016/j.biopha.2022.113500.

[3] V. Bellver-Landete, F. Bretheau, B. Mailhot, N. Vallières, M. Lessard, M.-E. Janelle, N. Vernoux, M.-È. Tremblay, T. Fuehrmann, M.S. Shoichet, S. Lacroix, Microglia are an essential component of the neuroprotective scar that forms after spinal cord injury, Nat. Commun. 10 (2019) 518, https://doi.org/10.1038/s41467-019-08446-0.

[4] F.H. Brennan, Y. Li, C. Wang, A. Ma, Q. Guo, Y. Li, N. Pukos, W.A. Campbell, K. G. Witcher, Z. Guan, K.A. Kigerl, J.C.E. Hall, J.P. Godbout, A.J. Fischer, D. M. McTigue, Z. He, Q. Ma, P.G. Popovich, Microglia coordinate cellular interactions during spinal cord repair in mice, Nat. Commun. 13 (2022) 4096, https://doi.org/10.1038/s41467-022-31797-0.

[5] A. Vidal-Itriago, R.A.W. Radford, J.A. Aramideh, C. Maurel, N.M. Scherer, E. K. Don, A. Lee, R.S. Chung, M.B. Graeber, M. Morsch, Microglia morphophysiological diversity and its implications for the CNS, Front. Immunol. 13 (2022). https://www.frontiersin.org/articles/10.3389/fimmu.2022.997786. (Accessed 30 October 2023).

[6] J.C.T. Chio, K.J. Xu, P. Popovich, S. David, M.G. Fehlings, Neuroimmunological therapies for treating spinal cord injury: evidence and future perspectives, Exp. Neurol. 341 (2021) 113704, https://doi.org/10.1016/j.expneurol.2021.113704.

[7] S. Papa, I. Caron, F. Rossi, P. Veglianese, Modulators of microglia: a patent review, Expert Opin. Ther. Pat. 26 (2016) 427–437, https://doi.org/10.1517/13543776.2016.1135901.

[8] S. Papa, F. Rossi, R. Ferrari, A. Mariani, M. De Paola, I. Caron, F. Fiordaliso, C. Bisighini, E. Sammali, C. Colombo, M. Gobbi, M. Canovi, J. Lucchetti, M. Peviani, M. Morbidelli, G. Forloni, G. Perale, D. Moscatelli, P. Veglianese, Selective nanovector mediated treatment of activated proinflammatory microglia/macrophages in spinal cord injury, ACS Nano 7 (2013) 9881–9895, https://doi.org/10.1021/nn4036014.

[9] S. Papa, I. Caron, E. Erba, N. Panini, M. De Paola, A. Mariani, C. Colombo, R. Ferrari, D. Pozzer, E.R. Zanier, F. Pischiutta, J. Lucchetti, A. Bassi, G. Valentini, G. Simonutti, F. Rossi, D. Moscatelli, G. Forloni, P. Veglianese, Early modulation of pro-inflammatory microglia by minocycline loaded nanoparticles confers long lasting protection after spinal cord injury, Biomaterials 75 (2016) 13–24, https://doi.org/10.1016/j.biomaterials.2015.10.015.

[10] S. Papa, I. Vismara, A. Mariani, M. Barilani, S. Rimondo, M. De Paola, N. Panini, E. Erba, E. Mauri, F. Rossi, G. Forloni, L. Lazzari, P. Veglianese, Mesenchymal stem cells encapsulated into biomimetic hydrogel scaffold gradually release CCL2 chemokine in situ preserving cytoarchitecture and promoting functional recovery in spinal cord injury, J. Contr. Release 278 (2018) 49–56, https://doi.org/10.1016/j.jconrel.2018.03.034.

[11] H.R.J. van Weering, T.W. Nijboer, M.L. Brummer, E.W.G.M. Boddeke, B.J.L. Eggen, Microglia morphotyping in the adult mouse CNS using hierarchical clustering on principal components reveals regional heterogeneity but no sexual dimorphism, Glia 71 (2023) 2356–2371, https://doi.org/10.1002/glia.24427.

[12] M. del M. Fernández-Arjona, J.M. Grondona, P. Granados-Durán, P. Fernández-Llebrez, M.D. López-Ávalos, Microglia morphological categorization in a rat model of neuroinflammation by hierarchical cluster and principal components analysis, Front. Cell. Neurosci. 11 (2017). https://www.frontiersin.org/articles/10.3389/fncel.2017.00235. (Accessed 12 May 2023).

[13] J. Leyh, S. Paeschke, B. Mages, D. Michalski, M. Nowicki, I. Bechmann, K. Winter, Classification of microglial morphological phenotypes using machine learning, Front. Cell. Neurosci. 15 (2021). https://www.frontiersin.org/articles/10.3389/fncel.2021.701673. (Accessed 1 February 2023).

[14] L. Mukherjee, M.A.K. Sagar, J.N. Ouellette, J.J. Watters, K.W. Eliceiri, A deep learning framework for classifying microglia activation state using morphology and intrinsic fluorescence lifetime data, Front. Neuroinf. 16 (2022). https://www.frontiersin.org/articles/10.3389/fninf.2022.1040008. (Accessed 6 December 2023).

[15] L. Stetzik, G. Mercado, L. Smith, S. George, E. Quansah, K. Luda, E. Schulz, L. Meyerdirk, A. Lindquist, A. Bergsma, R.G. Jones, L. Brundin, M.X. Henderson, J. A. Pospisilik, P. Brundin, A novel automated morphological analysis of Iba1+

microglia using a deep learning assisted model, Front. Cell. Neurosci. 16 (2022) 944875, https://doi.org/10.3389/fncel.2022.944875.
[16] J. Silburt, I. Aubert, MORPHIOUS: an unsupervised machine learning workflow to detect the activation of microglia and astrocytes, J. Neuroinflammation 19 (2022) 24, https://doi.org/10.1186/s12974-021-02376-9.
[17] S. Choi, D. Hill, L. Guo, R. Nicholas, D. Papadopoulos, M.F. Cordeiro, Automated characterisation of microglia in ageing mice using image processing and supervised machine learning algorithms, Sci. Rep. 12 (2022) 1806, https://doi.org/10.1038/s41598-022-05815-6.
[18] L. Möhle, P. Bascuñana, M. Brackhan, J. Pahnke, Development of deep learning models for microglia analyses in brain tissue using DeePathology^{TM} STUDIO, J. Neurosci. Methods 364 (2021) 109371, https://doi.org/10.1016/j.jneumeth.2021.109371.
[19] V. Veneruso, E. Petillo, F. Pizzetti, A. Orro, D. Comolli, M. De Paola, A. Verrillo, A. Baggiolini, S. Votano, F. Castiglione, M. Sponchioni, G. Forloni, F. Rossi, P. Veglianese, Synergistic pharmacological therapy to modulate glial cells in spinal cord injury, Adv Mater (2023) e2307747, https://doi.org/10.1002/adma.202307747.
[20] S. Papa, V. Veneruso, E. Mauri, G. Cremonesi, X. Mingaj, A. Mariani, M. De Paola, A. Rossetti, A. Sacchetti, F. Rossi, G. Forloni, P. Veglianese, Functionalized nanogel for treating activated astrocytes in spinal cord injury, J. Contr. Release 330 (2021) 218–228, https://doi.org/10.1016/j.jconrel.2020.12.006.
[21] E. Mauri, P. Veglianese, S. Papa, A. Rossetti, M. De Paola, A. Mariani, Z. Posel, P. Posocco, A. Sacchetti, F. Rossi, Effects of primary amine-based coatings on microglia internalization of nanogels, Colloids Surf. B Biointerfaces 185 (2020) 110574, https://doi.org/10.1016/j.colsurfb.2019.110574.
[22] O. Ronneberger, P. Fischer, T. Brox, U-net: convolutional networks for biomedical image segmentation, in: N. Navab, J. Hornegger, W.M. Wells, A.F. Frangi (Eds.), Medical Image Computing and Computer-Assisted Intervention – MICCAI 2015, Springer International Publishing, Cham, 2015, pp. 234–241, https://doi.org/10.1007/978-3-319-24574-4_28.
[23] Y. Sun, W. Zuo, P. Yun, H. Wang, M. Liu, FuseSeg: semantic segmentation of urban scenes based on RGB and thermal data fusion, IEEE Trans. Autom. Sci. Eng. 18 (2021) 1000–1011, https://doi.org/10.1109/TASE.2020.2993143.
[24] S.A. Bala, S. Kant, Dense dilated inception network for medical image segmentation, Int. J. Adv. Comput. Sci. Appl. 11 (2020), https://doi.org/10.14569/IJACSA.2020.0111195.
[25] A. Lou, S. Guan, M.H. Loew, DC-UNet: rethinking the U-Net architecture with dual channel efficient CNN for medical image segmentation, in: B.A. Landman, I. Išgum (Eds.), Medical Imaging 2021: Image Processing, Online Only, United States, SPIE, 2021, p. 98, https://doi.org/10.1117/12.2582338.
[26] J. Li, Z.L. Yu, Z. Gu, H. Liu, Y. Li, Dilated-inception net: multi-scale feature aggregation for cardiac right ventricle segmentation, IEEE Trans. Biomed. Eng. 66 (2019) 3499–3508, https://doi.org/10.1109/TBME.2019.2906667.
[27] B. Sankur, Survey over image thresholding techniques and quantitative performance evaluation, J. Electron. Imag. 13 (2004) 146, https://doi.org/10.1117/1.1631315.
[28] I. Vismara, S. Papa, V. Veneruso, E. Mauri, A. Mariani, M. De Paola, R. Affatato, A. Rossetti, M. Sponchioni, D. Moscatelli, A. Sacchetti, F. Rossi, G. Forloni, P. Veglianese, Selective modulation of A1 astrocytes by drug-loaded nanostructured gel in spinal cord injury, ACS Nano 14 (2020) 360–371, https://doi.org/10.1021/acsnano.9b05579.
[29] C. Macks, S.-J. Gwak, M. Lynn, J.S. Lee, Rolipram-loaded polymeric micelle nanoparticle reduces secondary injury after rat compression spinal cord injury, J. Neurotrauma 35 (2018) 582–592, https://doi.org/10.1089/neu.2017.5092.
[30] Y. Yin, B. Hu, X. Yuan, L. Cai, H. Gao, Q. Yang, Nanogel: a versatile nano-delivery system for biomedical applications, Pharmaceutics 12 (2020) E290, https://doi.org/10.3390/pharmaceutics12030290.
[31] F. Pinelli, Ó.F. Ortolà, P. Makvandi, G. Perale, F. Rossi, In vivo drug delivery applications of nanogels: a review, Nanomedicine (Lond) 15 (2020) 2707–2727, https://doi.org/10.2217/nnm-2020-0274.
[32] E.J. Bradbury, E.R. Burnside, Moving beyond the glial scar for spinal cord repair, Nat. Commun. 10 (2019) 3879, https://doi.org/10.1038/s41467-019-11707-7.
[33] G. Courtine, M.V. Sofroniew, Spinal cord repair: advances in biology and technology, Nat Med 25 (2019) 898–908, https://doi.org/10.1038/s41591-019-0475-6.
[34] T.M. O'Shea, J.E. Burda, M.V. Sofroniew, Cell biology of spinal cord injury and repair, J. Clin. Invest. 127 (2017) 3259–3270, https://doi.org/10.1172/JCI90608.
[35] A. Shafqat, I. Albalkhi, H.M. Magableh, T. Saleh, K. Alkattan, A. Yaqinuddin, Tackling the glial scar in spinal cord regeneration: new discoveries and future directions, Front. Cell. Neurosci. 17 (2023) 1180825, https://doi.org/10.3389/fncel.2023.1180825.
[36] J. Reddaway, P.E. Richardson, R.J. Bevan, J. Stoneman, M. Palombo, Microglial morphometric analysis: so many options, so little consistency, Front Neuroinform 17 (2023) 1211188, https://doi.org/10.3389/fninf.2023.1211188.
[37] S. Jung, J. Aliberti, P. Graemmel, M.J. Sunshine, G.W. Kreutzberg, A. Sher, D. R. Littman, Analysis of fractalkine receptor CX $_3$ CR1 function by targeted deletion and green fluorescent protein reporter gene insertion, Mol. Cell Biol. 20 (2000) 4106–4114, https://doi.org/10.1128/MCB.20.11.4106-4114.2000.